




Cite this: *Phys. Chem. Chem. Phys.*,
2019, 21, 19153

Moiré and honeycomb lattices through self-assembly of hard-core/soft-shell microgels: experiment and simulation†

Kirsten Volk,^a Florian Deißbeck,^b Suwendu Mandal,^b Hartmut Löwen^{*b} and Matthias Karg  ^{*a}

Control over microstructure and interparticle spacing in substrate-supported colloidal arrangements is a key challenge in colloidal self-assembly. We demonstrate here the preparation of Moiré and honeycomb monolayer lattices from core/shell microgels with rigid inorganic cores and soft, deformable hydrogel shells. These structures were realized by the sequential double deposition of freely floating monolayers from the air/water interface onto the same, centimetre-scale substrate. Due to the soft and deformable character of the hydrogel shells, the second applied monolayer fully settles into the same plane as the first monolayer. The resulting structural motif is determined by the drying conditions applied to the second deposition step. We support our experimental findings by Brownian dynamics simulations and provide insights into the structure formation process.

Received 2nd June 2019,
Accepted 12th August 2019

DOI: 10.1039/c9cp03116b

rsc.li/pccp

Introduction

Colloidal self-assembly has seen tremendous progress in recent years due to developments in the synthesis of colloids with size and shape control on the one hand and in self-assembly methods on the other hand.^{1–13} An ongoing challenge in this field is to fully explore the structural diversity that can be accessed by self-assembly of simple colloidal building blocks,^{14–19} ideally from stable “colloidal inks”. Furthermore, the application to functional colloids, *e.g.* noble metal nanoparticles that feature localised surface plasmon resonances (LSPRs), is relevant to fields such as light-management in thin-film solar cells,²⁰ fabrication of new optical metamaterials²¹ and sensors²² as well as 2D nanolasers.^{23–27} Control over surface coverage, homogeneity, inter-particle distance and periodicity are crucial criteria relevant to such applications.²⁰ An example for a versatile assembly strategy is interface-mediated assembly using *e.g.* air/water interfaces where initially hexagonal close packed arrays of hard colloids with large single crystalline domains were achieved.^{28–30} Recently this process was extended by Hummel *et al.* who showed that all five 2-dimensional Bravais lattices are accessible by transfer of particle monolayers from air/water interfaces onto substrates with defined contact angles.³¹ Here non-close packed assemblies became

accessible by the post-assembly lattice deformation. In contrast to the assembly of hard sphere colloids, soft particles have recently attracted a lot of attention due to their soft interaction potential^{32–35} and the resulting deformability.^{36,37}

Furthermore, it is possible to combine functional hard sphere-like colloids that feature *e.g.* plasmonic or fluorescent properties with soft polymer materials in form of well-defined core/shell colloids.^{38,39} In this case particle–particle interactions are determined by the soft polymer shell that also controls the inter-particle distance in assembly.²⁸

Volk *et al.* have shown that hydrogel encapsulated silver and gold nanoparticles can spontaneously self-assemble into hexagonally packed monolayers when floated at the air/water interface.¹⁴ The resulting structures showed a homogeneous surface coverage independent of the size and material of the employed plasmonic core. The interparticle distances were purely determined by the shell size and the time-dependent shell expansion at the air/water interface. Starting with interparticle distances close to the bulk hydrodynamic diameter right after deposition of the particles to the air/water interface, interfacial tension causes lateral deformation of the hydrogel shells leading to an increase in interparticle distance with time.

This assembly concept has been extended by Honold *et al.* who showed that the sequential double deposition of core/shell colloids from air/water interfaces onto solid supports can lead to binary monolayers with honeycomb structures.⁴⁰ Here the particles from the second deposition can settle into the large voids from the first deposition. Upon drying the shell shrinks to a much smaller size on the substrate leaving large voids in

^a Institut für Physikalische Chemie I: Kolloide und Nanooptik, Heinrich-Heine-Universität Düsseldorf, D-40225 Düsseldorf, Germany. E-mail: karg@hhu.de

^b Institut für Theoretische Physik II: Weiche Materie, Heinrich-Heine-Universität Düsseldorf, D-40225 Düsseldorf, Germany. E-mail: hlowen@thphy.uni-duesseldorf.de

† Electronic supplementary information (ESI) available. See DOI: 10.1039/c9cp03116b

between the particles. By the addition of the second monolayer additional functionality can be achieved either by new symmetries, particle properties or a combination of both. For example colloids with significantly smaller particle sizes can be deposited to give complex ABx structures as demonstrated by Fernández-Rodríguez using the Langmuir-trough technique.⁴¹

In this work, we elucidate the driving forces for the formation of 2D honeycomb and Moiré lattices of hard core/soft shell colloids. For the preparation of the ordered superstructures, we use a double deposition approach where two hexagonally ordered particle monolayers are assembled and transferred successively onto the same substrate. To do so we use the spontaneous self-assembly at air/water interfaces as the first and transfer from the interface to solid substrates as the second step. The final superstructure created by the two hexagonal monolayers can be controlled by the applied drying conditions. Slow drying leads to 2D honeycomb assemblies whereas fast drying results in 2D Moiré structures. Brownian dynamics simulations are used to explain the experimental findings and the resulting 2D assemblies. In particular, our study confirms that different structures (Moiré or honeycomb) are the sole consequence of different equilibration times rather than capillary forces, which are strong enough to deform the polymer shell.

Experimental section

Chemicals and materials

Gold(III) chloride trihydrate (Sigma-Aldrich, $\geq 99.9\%$), sodium citrate dihydrate (Sigma-Aldrich, $\geq 99\%$), butenylamine hydrochloride (Sigma-Aldrich, 97%), sodium dodecyl sulfate (Merck), *N*-isopropylacrylamide (NIPAM; Sigma-Aldrich, 97%), *N,N'*-methylenebisacrylamide (BIS; Sigma-Aldrich, 99%), potassium peroxydisulfate (Fluka, $\geq 99\%$), silver nitrate (99.999%, Sigma), ascorbic acid (p.a., Roth), acetonitrile (HPLC grade, Fisher Chemicals), ethanol (p.a., Honeywell) and Hellmanex III (Hellma GmbH) were used as received. Purified water (MQ-water) from a Milli-Q system (Millipore) with a final resistivity of 18.2 M Ω cm was used for all synthesis, purification and assembly steps. Microscope glass slides of 1 mm thickness (Menzel-Gläser, Thermo Scientific) were cut in pieces of approximately 1 \times 1 cm² and used as substrates for the particle assemblies.

Synthesis of core/shell microgels

The core/shell particles were synthesised in three steps, which are all easy to scale up in order to produce large quantities. First gold nanoparticles were synthesised according to the well-established Turkevich method.⁴² In the second step, these rigid nanoparticles were encapsulated in a cross-linked poly(*N*-isopropylacrylamide) (PNIPAM) shell by seeded precipitation polymerisation following a well-established protocol.⁴³ The polymerisation was performed with a monomer concentration $c(\text{NIPAM}) = 0.06$ M and a nominal cross-linker (BIS) concentration of 15% with respect to the monomer NIPAM. After these

steps core/shell particles with spherical cores of approximately 14 nm in diameter and hydrogel shells with an overall hydrodynamic diameter of 347 nm (20 °C, swollen state) were obtained. In a third step the cores of these core/shell particles were overgrown with silver (Ag). In order to obtain Ag-PNIPAM particles with 100 nm silver cores, a previously published protocol by Volk *et al.* was used.⁴⁴ Therefore, an ice-cold mixture of 2.65 mL MQ water and 0.5 mL acetonitrile was prepared in a round-bottom-flask. Then 79 μL of the core/shell particles (2 wt%), 2 mL of an ice-cold, aqueous ascorbic acid solution (49 mM) and 5.05 mL of a silver nitrate solution (15 mM) were added under stirring one after another. The reaction was allowed to proceed for 30 minutes before warming up to room temperature. The resulting particles were separated from dispersion by centrifugation at 2400 rcf for 25 min until the supernatant was completely colourless. After removal of the supernatant, the particles were redispersed in ethanol. This process was repeated three times for purification purposes. The concentration of the purified particles was determined gravimetrically and adjusted to approximately 1 wt%.

Interface-assisted assembly and double deposition

First, glass substrates were cleaned by sonication for 15 min in an aqueous Hellmanex solution (2 vol%). After that the substrates were rinsed with and further sonicated in water. Finally sonication in ethanol for 15 min was applied. After rinsing with ethanol, the substrates were dried with compressed, dry nitrogen. The core/shell particles were assembled at the air/water interface by dispensing a particle dispersion onto the water surface. Therefore, a crystallising dish (6 cm in diameter) was filled with MQ water and approximately 7 μL of a 1 wt% particle dispersion in ethanol was applied using an Eppendorf pipette. The freely floating particle monolayers were transferred onto 1 cm² glass substrates by careful immersion of the substrate below the particle monolayer and slow retraction at a 45° angle through the floating particle monolayer. The centre-to-centre distance was adjusted by the dwell-time of the monolayer at the air/water interface following the kinetics reported by us previously.¹⁴ The coated glass substrates were then carefully dried by blowing with a heatgun against the back of the substrate. For this a Steinel HL 1920E heatgun with a tunable temperature control between 80 °C and 600 °C (continuously variable with steps 1–9) was employed. The temperature was set to 7 and the fan to stage 3 (300–500 L min⁻¹). The sample was placed directly at the nozzle of the heatgun to avoid turbulences on the substrate. After approximately 10 s, the entire monolayer was dry including the accumulated water at the lower edge of the substrate. The main area of the monolayer was already dry after 3–5 s. Honeycomb and Moiré arrays were prepared by sequential deposition of two hexagonal particle monolayers onto the same substrate. For the application of the second monolayer, the substrate that was already coated once was treated with a heatgun for 10 s and with O₂ plasma for 15 s just before use. These steps were found to be crucial to attach the particles more firmly to the substrate and to enhance the hydrophilicity of the substrate. Then the substrate was immersed vertically into a crystallising dish

which was filled with fresh MQ water. For this the substrate was clamped between self-looking tweezers and hung on a stand arm. Next a fresh particle monolayer was prepared at the air/water interface using the same method as above while the substrate was completely immersed in the aqueous phase. Slow, vertical retraction (90° with respect to the air/water interface) of the substrate by hand (approximately 10 s) through the particle monolayer lead to the deposition of the second monolayer. To obtain honeycomb structures, the withdrawn sample was left to dry slowly under ambient conditions. It took 5 minutes for the monolayer to dry and 10 minutes until also the lower edge had dried completely. For Moiré structures fast drying using a heatgun with the same settings as above (10 s) was employed.

Atomic force microscopy

1024×1024 pixel² topographic AFM images ($10 \times 10 \mu\text{m}^2$) were recorded with a Nanowizard 4 (JPK Instruments) in intermittent contact mode against air. OTESPA-R3 AFM probes (Bruker) were employed for imaging. The cantilevers had a nominal resonance frequency of 300 kHz and a spring constant of 26 N m^{-1} . The tip geometry was as visible apex with a nominal tip radius of 7 nm. The recorded height images were tilt-corrected using a polynomial line fit in the JPK SPM Data Processing software. The freely available ImageJ software was used to transform the color image into gray scale and thereof determine the centre of each particle in xy -coordinates. This information was then used to determine the centre-to-centre distance d_{c-c} and radial distribution function (RDF) of the particle monolayer.

Transmission electron microscopy

A Zeiss CEM902 transmission electron microscope with 80 kV acceleration voltage operated in bright-field mode was used to characterize the core/shell particles in terms of size and morphology. The sample was prepared on a carbon coated copper grid by applying a diluted droplet of the purified particle dispersion onto the grid. It was left to dry under ambient conditions. Image analysis was performed using the software ImageJ.

Brownian dynamics simulation

To gain more quantitative insights into the experimentally observed Moiré and honeycomb structures, we perform BD simulations. We use a square-shoulder potential^{45–49} to model these core/shell microgel particles using a hard core diameter σ surrounded by a soft shell with a total diameter $\lambda\sigma$ as illustrated in Fig. 1a. Thus, λ indicates the ratio between the outer soft shell and the inner hard core diameter. Following the work of Schoberth *et al.*,⁵⁰ we write the square-shoulder potential as

$$u(r) = \begin{cases} u_c(r) + u_f(r) & r < 1 + w \\ u_f(r) & 1 + w \leq r \end{cases} \quad (1)$$

with

$$u_f(r) = \frac{\varepsilon}{2} \left(1 + \tanh\left(\frac{\lambda - r}{w}\right) \right) \quad (2)$$

for the flat shoulder, and

$$u_c(r) = h\varepsilon \left(\frac{r - 1}{w} - 1 \right)^4 \quad (3)$$

for the hard core, where ε corresponds to the pair interaction energy, w denotes the width of the potential at the shell-shell contact, and h is the shoulder height. We consider $\lambda = 3.44$, which indicates the ratio of the soft shell diameter and the core diameter of a microgel particle in experiments. For simplicity, we set $w = 0.03$ and $h = 0.543$. The choice of w and h was to ensure the potential has a smooth gradient at the outer shell, and a strong repulsive force at the inner core. For parameters in the same range, the results do not change qualitatively. In fact, the actual values for w and h , however, do not possess any direct physical significance. A sketch of the potential $u(r)$ is shown in Fig. 1b. One observes a flat shoulder between distance σ and $\lambda\sigma$, where the particles do not feel any forces. Within our model, we can estimate a critical force barrier ($F_{\text{crit}} = 7k_{\text{B}}T/\sigma$) for the shell-shell overlapping, see the inset in Fig. 1b.

Fig. 1c shows a schematic illustration of a bilayer system, where the bottom hexagonal layer is always fixed. Another hexagonal monolayer at a given rotation angle $\alpha = 30^\circ$ is positioned above the bottom layer, see also Fig. 3f for side-view. Next, to mimic the drying process of the experiments,

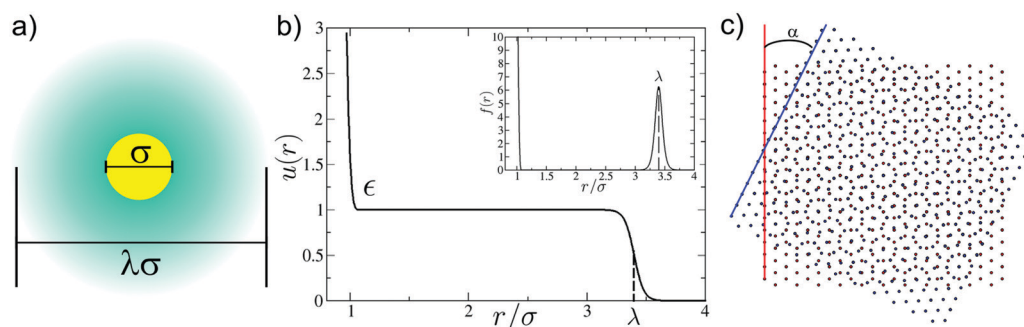


Fig. 1 (a) Schematic representation of the core/shell microgel particles. (b) Square-shoulder potential having two characteristic length scales, namely, the hard core diameter σ and the total core/shell diameter $\lambda\sigma$. Inset: The radial part of the force $f(r)$ derived from $u(r)$. The dashed line illustrates the force at the shell-shell contact. (c) A typical illustration of rotation angle $\alpha = 30^\circ$ between two hexagonal layers.

a constant force F_{ext} (towards the negative z direction) is applied to the top hexagonal layer. Accordingly, particle positions r_i of the top layer evolve as

$$\dot{r}_i(t) = \frac{D_0}{k_B T} [-\nabla_i u(r) + \mathbf{F}_{\text{ext}}] + \sqrt{2D_0} \mathbf{R}_i(t) \quad (4)$$

where D_0 denotes the short-time diffusion coefficient and $\mathbf{R}_i(t)$ is Gaussian white noise with zero mean and unit variance:

$$\langle \mathbf{R}_i(t) \mathbf{R}_j(t') \rangle = \delta_{ij} \delta(t - t') \quad (5)$$

To obtain a straightforward comparison with experiments, we have used $\lambda\sigma = 347$ nm and $D_0 = 1.2 \times 10^{-12}$ m² s⁻¹.⁵¹ We have further set $\varepsilon = k_B T$ and $t_0 = \lambda^2 \sigma^2 / D_0 = 0.1$ s respectively, as the units of energy scale and time scale. The equation of motion has been integrated with a finite time step $dt = 10^{-4} t_0$ using the Euler method, see ref. 52. Periodic boundary conditions are used in both x and y directions. Each simulation is performed up to 5 million time steps, which is equivalent to a total simulation time $t = 60$ seconds, in a box of size $L_x = 200\lambda\sigma$, $L_y = 200\lambda\sigma$, and $L_z = 2.5\lambda\sigma$.

Depending on the strength of the external force, one can observe interesting behaviours. For example, the soft shells do not overlap subjected to a small external force ($F_{\text{ext}} < 7k_B T / \sigma$), whereas for a large external force ($F_{\text{ext}} \gg 7k_B T / \sigma$) the soft shells entirely overlap and the core repulsion dominates. At an intermediate external force, the soft shells can overlap partially.

Results & discussion

Structure of colloids in dispersion and adsorbed on solid substrates

In this work core/shell colloids with silver nanoparticle cores and soft hydrogel shells based on chemically cross-linked poly(*N*-isopropylacrylamide) (PNIPAM) were self-assembled into periodic 2D arrays. Fig. 2a shows a representative bright-field transmission electron microscopy (TEM) image of the colloids. The nearly spherical silver cores can be nicely distinguished from the hydrogel shells that are visible as grey corona around the cores due to the different electron densities. The mean diameter of the cores determined from several TEM images is $d_{\text{core}} = 101 \pm 10$ nm. The slight deviation from a perfect spherical shape is mainly attributed to the multicrystalline nature of the employed seed particles. The various crystal facets determine the overgrowth. This together with the polydispersity of about 10% leads to a slight broadening of the LSPR of the plasmonic particles and less pronounced quadrupolar mode as compared to the perfectly spherical and monodisperse particles.⁴⁴ The core quality however, does not impact the quality of the assembly since this is determined by the hydrogel shell. Related to the high vacuum in the TEM chamber, the hydrogel shells are imaged in their dry state and are therefore almost fully collapsed. Consequently, the shells appear much thinner than in the dispersed state, which is the relevant situation during particle assembly. The overall particle dimensions in dilute aqueous dispersion were determined by dynamic light scattering (DLS) in dependence of the

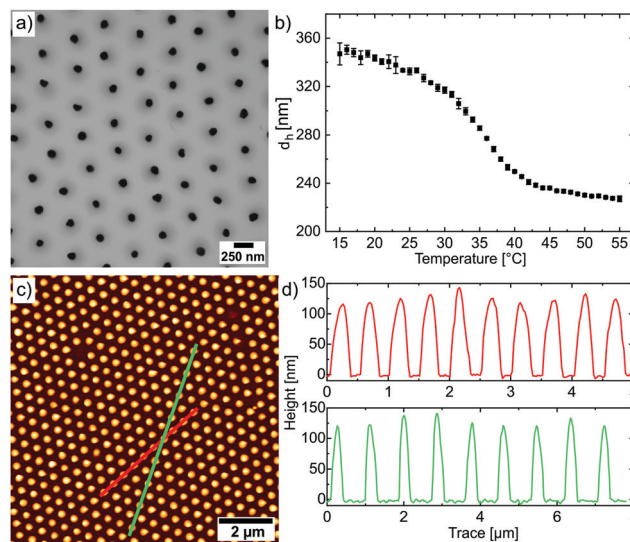


Fig. 2 Characterisation of the hard core/soft shell Ag–PNIPAM particles. (a) Bright-field TEM image showing the particles in the dry state. (b) Evolution of the hydrodynamic diameter d_h with temperature in aqueous dispersion. The VPT temperature is at approximately 34 °C. (c) AFM image of a hexagonally ordered particle monolayer with $d_{c-c} = 485 \pm 23$ nm obtained from a single deposition step. (d) Cross-sections from AFM height images generated along the red and green lines in (c).

dispersion temperature (Fig. 2b). Due to the volume phase transition (VPT) of the PNIPAM shell, a continuous decrease of the overall hydrodynamic diameter with increasing temperature is observed in the vicinity of the VPT temperature. This change in overall size is related to the shrinkage of the hydrogel shell upon release of water at poor solvent conditions.^{53–56} In the fully swollen state, we determine $d_h(\text{swollen}) = 347 \pm 2$ nm (average for data of 15–19 °C), while the fully collapsed state yields $d_h(\text{collapsed}) = 228 \pm 1$ nm (average for data of 51–55 °C). Taking into account the diameter of the non-responsive cores, this implies a decrease of the shell thickness by almost a factor of two (from 123 to 64 nm). The VPT temperature is approximately at 34 °C as determined from the point of inflection of the deswelling curve. Using the core dimensions and the total hydrodynamic diameter d_h we calculate shell-to-core ratios $\lambda = d_h/d_{\text{core}}$ of 3.44 for the fully swollen state and 2.26 for the fully collapsed state. The core/shell particles were used for self-assembly at the air/water interface where freely-floating highly periodic monolayers are formed spontaneously.¹⁴ This spontaneous self-assembly is the result of attractive capillary interactions that occur due to local deformations of the air/water interface by the adsorbed core/shell microgels.^{57,58} The initial centre-to-centre distance of this monolayer is mainly determined by the hydrodynamic diameter of the core/shell particles. With increasing dwell-time at the air/water interface, the hydrogel shells slowly stretch out laterally driven by interfacial tension.⁵⁹ In consequence a continuous increase in the centre-to-centre distance occurs. Knowing the kinetics of this process from a previous study allows us to choose a certain centre-to-centre distance for the monolayer deposition onto the substrate.¹⁴ Fig. 2c shows an

AFM height profile recorded from such a monolayer upon transfer on a solid substrate. Because the image was recorded in the dry state of the monolayer against air, the hydrogel shells are in a collapsed state resulting in the non-close packed appearance of the monolayer. Despite this drying of the shells, the particles are arranged in a hexagonal lattice with a nearest neighbour centre-to-centre distance of $d_{c-c} = 485 \pm 23$ nm. When the particles are transferred to the substrate they still possess their swollen and deformed dimensions but once the polymer is dried the remaining particle footprint on the substrate becomes much smaller. It has been shown that dry core/shell particles then adapt a fried-egg like morphology on the substrate.⁶⁰ The resulting spacing in between the particles is clearly visible in the cross-sectional traces in Fig. 2d. The average particle diameter in this dry state is $d_{dry} = 330$ nm. The void in a triplet of neighbouring particles in the hexagonal monolayer can accommodate a sphere with a diameter d_{void} according to:

$$d_{void} = \frac{2}{\sqrt{3}}d_{c-c} - d_{dry} \quad (6)$$

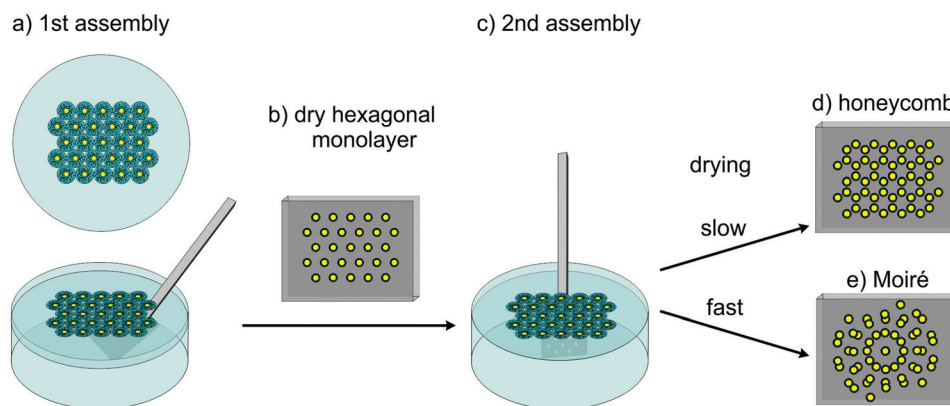
Details on the derivation of eqn (6) and a schematic depiction illustrating the void space can be found in Fig. S1 (ESI[†]). Using the experimentally determined values for d_{dry} and d_{c-c} one can calculate $d_{void} = 230$ nm. This value is much smaller than the

hydrodynamic diameter in bulk (swollen state) and also significantly smaller than the dry state diameter d_{dry} . Thus only colloids that have a pronounced softness and that can undergo large deformation can penetrate into this void space.

Assembly process and simulation conditions

Fig. 3 schematically depicts the two sequential self-assembly steps and the structures of the resulting monolayers. A first monolayer is prepared at the air/water interface and subsequently transferred onto a glass substrate by retracting the glass substrate through the monolayer at an angle of 45° (for details see Experimental section). Upon drying, the hydrogel shells collapse around the hard core resulting in a non-close packed, hexagonally ordered particle monolayer (see Fig. 2c and 3b). For the second monolayer deposition, the substrate coated with the first monolayer is submerged into water before depositing a fresh monolayer at the air/water interface above (Fig. 3c). Then the substrate is carefully withdrawn vertically through the second monolayer at the interface. The change in the retraction procedure has two reasons. First, the coated substrate needs to be submerged into the aqueous phase before the new monolayer is applied because otherwise particles would attach during the immersion process. Hanging the sample vertically was therefore the obvious choice. Secondly, we wanted to move/tilt the sample the least possible way during retraction and

Experimental preparation procedure



Simulation procedure

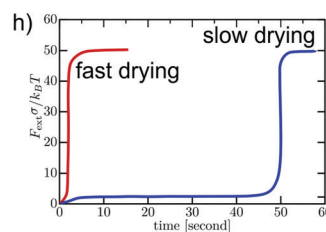
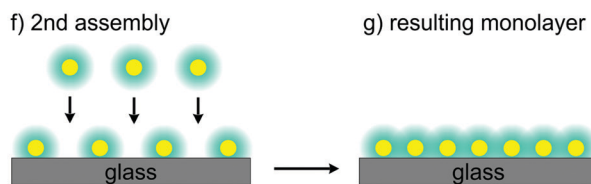


Fig. 3 Top: Sketch of the self-assembly process for honeycomb and Moiré structures from left to right: (a) 1st assembly step: crystallising dish with hexagonally ordered, swollen core/shell colloids at the air/water interface (top view) and immersed glass substrate below monolayer (side view). (b) In the dried state, the monolayer features non-close packed hexagonal order due to shrinkage of the hydrogel shell (dry hexagonal monolayer). (c) 2nd assembly step: the coated substrate is immersed into water before the second monolayer is assembled and withdrawn onto the substrate carrying the first monolayer. (d) Slow drying of the particle array leads to the formation of honeycomb structures and fast drying to (e) Moiré structures. Bottom: Side view of the Brownian dynamics simulation protocol: (f) a particle layer (hexagonally ordered) is attached to the glass substrate and has no translational motion. Another hexagonal layer is placed above the bottom layer. A constant external force imposed on the top hexagonal layer squeezes these two layers into one monolayer (g). Two different protocols are presented to explain fast and slow drying processes in simulations (h).

drying in order to achieve reproducible drying conditions for every prepared sample. After this second transfer step, two different monolayer structures are observed depending on the drying conditions: when the second monolayer is dried slowly in the course of 5 minutes, honeycomb structures are formed (d). Rapid drying within 3–5 seconds on the other hand results in the formation of Moiré structures (e). The bottom row of Fig. 3 shows a schematic illustration of the Brownian dynamics (BD) simulation procedure is depicted in side-view. A hexagonally ordered monolayer is immobilised on the solid substrate and a second monolayer is placed above the bottom layer (f). Then a constant external force is imposed onto the mobile top layer. Consequently, the top layer is squeezed into the plane of the attached monolayer on the glass surface (g). Depending on the protocol used for the time-dependence of the external force, slow and fast drying can be mimicked and either honeycomb or Moiré structures are obtained, see Fig. 3h.

Comparison of microstructures from experiment and simulation

Fig. 4 shows the results from a second monolayer deposition on top of the first, hexagonally ordered monolayer depicted in Fig. 2c. In Fig. S2 (ESI[†]) the individual sublattices are highlighted in red and blue colour for easier illustration. For the sample with a honeycomb microstructure (Fig. 4a) slow drying conditions were applied whereas the Moiré structure in Fig. 4d is the result from fast drying using a heatgun. The honeycomb structure is visible over the whole AFM image and is only

disrupted at domain boundaries. These occur due to the self-assembly process which inherently produces some point and line defects. Furthermore, the individual hexagonal sublattices are multidomain structures consisting of smaller single crystal-line domains with different orientations. These characteristics also translate into the monolayers obtained from the double deposition process, *i.e.* also the honeycomb lattice is a multidomain sample. Analysis using fast Fourier transformation (FFT) of the real space particle positions nevertheless demonstrates the long range order of the honeycomb microstructure by the occurrence of multiple orders of Bragg peaks (Fig. 4b). Since the honeycomb structure is formed by the settlement of the particles of the second hexagonally ordered monolayer into the voids presented by three particles of the first monolayer,⁴⁰ the honeycomb structure is characterised by a hexagonal symmetry reflected by the six-fold symmetry of the Bragg peaks in the FFT. Taking into account the void space ($d_{\text{void}} = 230$ nm, eqn (6)), it becomes clear that the hydrogel shells undergo significant deformation in the honeycomb lattice. Now we compare the experimentally produced microstructure to the results from BD simulations depicted in Fig. 4c. Here a perfect honeycomb microstructure obtained by mimicking the slow drying process is shown. To compare the experimental and simulated structure, we calculate the radial distribution function (RDF) from xy -coordinates of the particle centre positions in the real space AFM images and structures obtained from BD simulations (inset in Fig. 4b). The RDF describes the average particle density around a central particle as a function of the

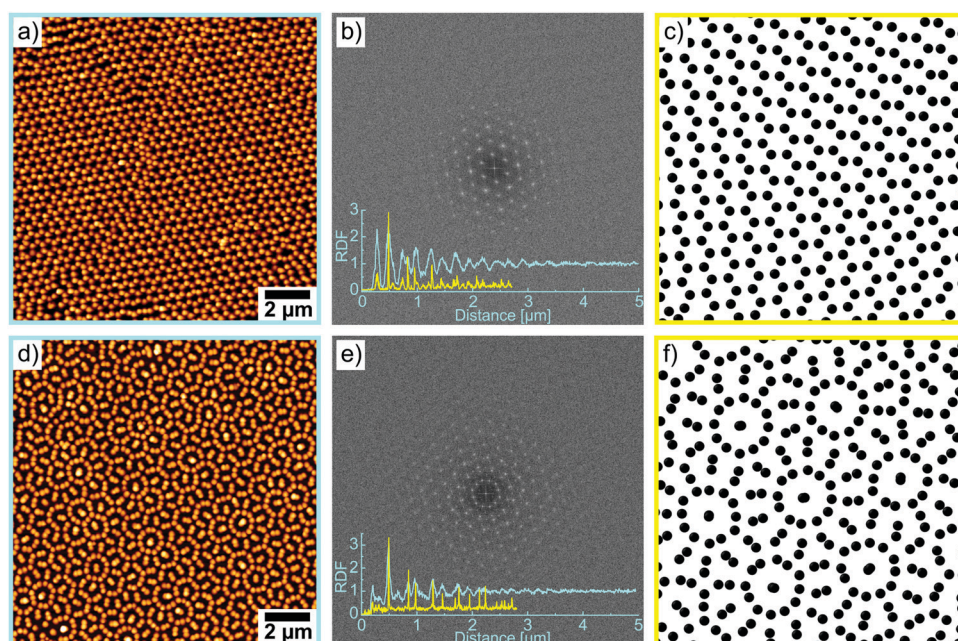


Fig. 4 Comparison of the experimentally observed microstructures to results from theoretical simulation. (a) AFM height image of a honeycomb monolayer obtained by slow drying of the second monolayer on top of the first one. (b) FFT of experimental honeycomb structure and RDFs of experimental (blue trace) and calculated (yellow trace) honeycomb structure as inset. (c) Honeycomb microstructure as a result from BD simulations. (d) AFM height image of a Moiré monolayer prepared by fast drying of the second monolayer on top of the first monolayer. (e) FFT of experimental Moiré structure and RDFs of experimental (blue trace) and calculated (yellow trace) Moiré structure as inset. (f) Moiré microstructure as a result from BD simulations with $\alpha = 30^\circ$.

radial distance^{58,61} and therefore can help to identify regular patterns. When an increase in particle density at a certain distance from a chosen centre particle is detected a peak in the RDF will occur. The RDF is an averaged response over all the particles in the monolayer. We can see a good match of the RDF traces from experiment (blue RDF) and simulated monolayer (yellow RDF) with only deviations in intensity and peak width. These deviations are explained by some degree of positional disorder and the presence of domain boundaries in the experimental sample as compared to the perfect structure from simulation.

Next the same analysis is performed for the experimental Moiré structure depicted in Fig. 4d. The FFT (Fig. 4e) shows multiple orders of Bragg peaks again indicating a long range order. The 12-fold symmetry points to a rotational offset between the first and second deposited hexagonally ordered particle monolayer. This is confirmed by the matching structure obtained from BD simulations when a rotation angle $\alpha = 30^\circ$ is employed for structure formation (Fig. 4f). For closer comparison RDFs are given as insets in Fig. 4e. Again a good match of the traces is found with deviations in peak width and intensity due to the imperfect experimental microstructure. Since we use fast drying conditions the particles from the second deposition step cannot settle slowly into the voids presented by the firstly deposited monolayer but are pushed into the first lattice with the orientation they possess at the air/water interface in regard to the monolayer attached to the glass. Consequently, the initial orientation of the two monolayers determines which Moiré motif is formed. Since we cannot control this orientation in experiment, samples with other Moiré motifs corresponding to different rotation angles between the first and the second layer were obtained. Some examples are shown in Fig. S3 (ESI†).

In order to show that our monolayers from the sequential double deposition are real 2D structures rather than an AB stacking of two monolayers as previously reported for example for hard spheres,⁶² we provide AFM cross-sections for the Moiré and honeycomb assemblies (Fig. 5a). The green cross-section profile corresponds to the hexagonal monolayer after the first deposition onto the solid substrate (see Fig. 2d) and is included for better comparison. The average maximum height of the

particles in this monolayer is approximately 125 nm and all particles sit in the same plane on the substrate. The cross-sections in red and blue were measured from the honeycomb lattice (red) and the Moiré lattice (blue) along straight lines as illustrated in the AFM height images in Fig. 5b and c. The average maximum height in the Moiré and honeycomb lattices are very similar to the ones determined for the single hexagonal monolayer and again all particles sit in the same plane on the substrate. This highlights that we indeed deal with real 2D structures, *i.e.* particle monolayers. Slight variations in particle height can be mainly attributed to the fact that the cross-section does not always go directly through the centre of the particles due to a particle arrangement that does not follow a straight line (particularly the Moiré pattern). Only when a particle from the first and second monolayer would settle in the same spot due to the given Moiré motif, the second particle sits on top of a particle of the first layer. Since the particle cannot occupy the same place in the 2D lattice as the first particle, the 2D pattern is broken in this particular position (Fig. S4, ESI†).

Before we discuss the simulation results, we make a clear distinction between the fast and the slow drying process in simulations: a setup that is dried by rapid heating will experience a large external force ($F_{\text{ext}} = 50k_{\text{B}}T/\sigma$) within a couple of seconds, whereas in a slow drying process we let the system to equilibrate for 50 seconds and then apply a large external force ($F_{\text{ext}} = 50k_{\text{B}}T/\sigma$), see Fig. 3h.

During the drying process, the normal component of capillary forces (F_{cap}) is balanced by the frictional drag force and the repulsive forces (F_{rep}) originating from the bottom layer, leading to the following equation

$$F_{\text{cap}} = \gamma\nu + F_{\text{rep}} \quad (7)$$

where $\gamma = k_{\text{B}}T/D_0$ is the Stokes friction coefficient of each particle and ν is the velocity of the drying front. From the experimental findings for ν and D_0 , we calculate that the drag force ($\gamma\nu$) is of the order of $1.0k_{\text{B}}T/\sigma$. Furthermore, we know that each particle requires about $7k_{\text{B}}T/\sigma$ for the shell-shell overlapping, see the inset of Fig. 1b. Since there are at least 4 neighboring particles, the total repulsive force should be about $F_{\text{rep}} \sim 28k_{\text{B}}T/\sigma$. Therefore, we chose the normal component of capillary forces $F_{\text{cap}} = 50k_{\text{B}}T/\sigma$ in our simulations to ensure the perfect penetration of the drying front into the bottom layer. As long as F_{ext} is larger than $30k_{\text{B}}T/\sigma$, the actual value does not matter as revealed by our simulations.

In order to study a Moiré structure formation, the highly packed (2D packing fraction = 0.9) top hexagonal layer rotated by an angle $\alpha = 30^\circ$ is placed above the highly packed bottom layer. Subsequent application of a large external force ($F_{\text{ext}} = 50k_{\text{B}}T/\sigma$) overcomes the force barrier required for the shell-shell overlapping, and eventually squeezes these two layers into one monolayer. This is equivalent to a fast drying process in experiments. Similar to experiments, the resulting monolayer shows a 12-fold symmetry (Moiré structure), in particular, one centre particle is surrounded by 12 particles at equal distance, see Fig. 4f. For clarity, we only plot the hard-core diameter of the microgel particles in Fig. 4. We also notice that there are

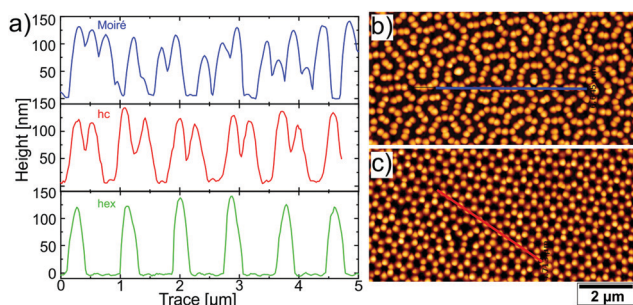


Fig. 5 Cross-section analysis of different monolayers. (a) Experimental cross-sections for single hexagonal monolayer (green), honeycomb (hc) lattice (red) and Moiré lattice (blue). (b and c) Corresponding AFM height images with the traces (solid lines) used for the cross-section analysis in (a).

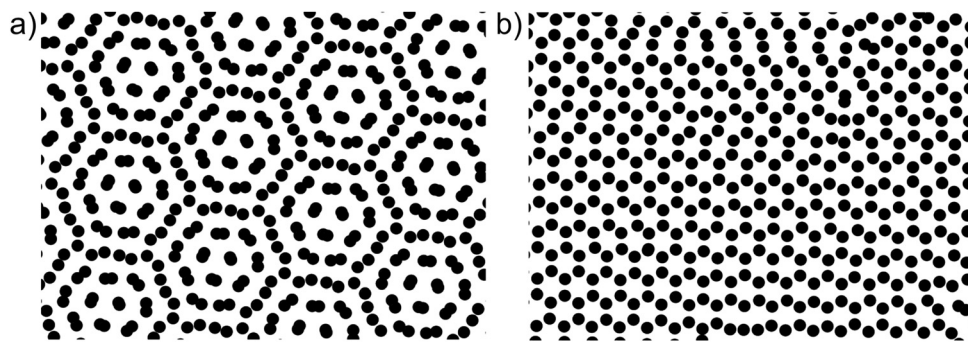


Fig. 6 (a) Two highly packed hexagonal layers with rotation angle of 13° . For simplicity, we plot only the core diameters of the microgel particles. (b) The final configuration after an equilibration time of 50 seconds. The particles of the top layers rearrange from 13° to 2° .

two particles at the centre of each Moiré pattern, and one of them remains outside the 2D plane, which is also in line with experimental observations, see Fig. 4d and height trace in Fig. S4 of the ESI.† This is expected because two hard cores cannot overlap.

To realise the slow drying process, we use the previous bilayer configuration with a rotation angle of $\alpha = 30^\circ$, and then allow the system to equilibrate in the course of 50 seconds. During this equilibration process, we apply a small external force ($F_{\text{ext}} = 1k_B T/\sigma$) on the top layer so that particles from both layers can interact without overlapping. Interestingly, we observe a structural transition of the top layer particles due to the soft nature of the shells, in particular, particles of the top layer rotate from 30° to 2° . This indicates that particles in the top layer try to adapt the configuration of the immobile bottom layer. In fact, this structural transition is valid for any starting rotation angle α . As an example, we present a structural transition from 13° to 2° in Fig. 6. At the end of this structural transition, we again apply a large external force ($F_{\text{ext}} = 50k_B T/\sigma$) to the top layer, and obtain honeycomb structures in the 2D plane with 6-fold symmetry, see Fig. 4a–c. Hence, a good agreement is found between experiments and simulations for different drying processes, which makes it possible to create mechanically stable honeycomb (slow drying) or Moiré (fast drying) structures in the 2D plane using a highly packed hexagonal bilayer system.

To provide robustness of our protocol, we also increase the shoulder width from $\lambda = 1.3$ to $\lambda = 4$, and obtain similar results. However, for $\lambda < 1.1$, hard core interactions dominate, and therefore it is not possible to squeeze a highly packed (2D packing fraction = 0.9) hexagonal bilayer into a monolayer. This further highlights that particles with two length scales are necessary to form mechanically stable honeycomb or Moiré structures in the 2D plane.

Conclusions

Core/shell microgels with rigid cores and soft, deformable hydrogel shells spontaneously self-assemble at air/water interfaces due to attractive capillary interactions. The resulting freely floating monolayers are characterised by a hexagonal arrangement of the

microgels with centre-to-centre distances that are governed by the thickness and swelling state of the hydrogel shells. Upon transfer onto a solid substrate – in our case glass – centimetre-scale, homogeneous coatings with large, single crystalline domains are obtained. Subsequent double deposition of monolayers onto the same substrate gives access to more complex 2-dimensional structures. Slow drying of the second on top of the first monolayer yields honeycomb lattices. In contrast, fast drying reveals Moiré lattices. In the latter case the exact structure is determined by the rotation angle between the domains of the first and the second monolayer. Because of the multidomain character of the hexagonal sublattices, Moiré structures with various rotation angles are found on the same substrate. All observed lattices are real 2-dimensional monolayers which means that all particles settle into the same lattice plane. This is the result of significant shell deformation and evidenced by cross-sectional analysis using atomic force microscopy.

Brownian dynamics simulations of the double deposition process support our experimental findings. Most importantly the simulations show that the fast drying conditions in experiment lead to Moiré structures as a non-equilibrium deposition, that is, when the second layer is squeezed into the first layer at sufficiently large forces. Contrary, rearrangement of the particle in the second monolayer occurs under equilibrium conditions corresponding to slow drying in experiment, leading to honeycomb lattices.

The present work resembles an important step toward surface nanostructuring using soft colloids. In future it would be interesting to study assembly of soft anisotropic colloids.^{63–68}

Conflicts of interest

There are no conflicts to declare.

Acknowledgements

This work was supported by the Deutsche Forschungsgemeinschaft (DFG) through the Emmy Noether programme (DFG, grant no. KA3880/1-1) and DFG, grant no. LO 448/22-1. K. V. acknowledges funding from the Fonds der Chemischen

Industrie (FCI) through the Verband der Chemischen Industrie e.V. (VCI) and support from the Elite Network of Bavaria (ENB). The authors like to thank Dr Tobias Honold for initial experiments on the sequential double deposition and fruitful discussions.

References

- N. Vogel, M. Retsch, C. A. Fustin, A. Del Campo and U. Jonas, *Chem. Rev.*, 2015, **115**, 6265–6311.
- T. Waltmann, C. Waltmann, N. Horst and A. Travesset, *J. Am. Chem. Soc.*, 2018, **140**, 8236–8245.
- X. Zha and A. Travesset, *J. Phys. Chem. C*, 2018, **122**, 23153–23164.
- R. K. Cersonsky, J. Dshemuchadse, J. Antonaglia, G. van Anders and S. C. Glotzer, *Phys. Rev. Mater.*, 2018, **2**, 125201.
- J. Zhang, Y. Li, X. Zhang and B. Yang, *Adv. Mater.*, 2010, **22**, 4249–4269.
- G. B. Sukhorukov, E. Donath, H. Lichtenfeld, E. Knippel, M. Knippel, A. Budde and H. Möhwald, *Colloids Surf., A*, 1998, **137**, 253–266.
- A. V. Tkachenko, *Phys. Rev. Lett.*, 2002, **89**, 148303.
- D. Y. Wang and H. Möhwald, *J. Mater. Chem.*, 2004, **14**, 459–468.
- S. Sacanna, D. J. Pine and G. R. Yi, *Soft Matter*, 2013, **9**, 8096–8106.
- F. Romano and F. Sciortino, *Nat. Mater.*, 2011, **10**, 171–173.
- Q. Chen, S. C. Bae and S. Granick, *Nature*, 2011, **469**, 381–384.
- H. B. Eral, D. M. Augustine, M. H. G. Duits and F. Mugele, *Soft Matter*, 2011, **7**, 4954–4958.
- J. P. S. Fitzgerald and M. Karg, *Phys. Status Solidi A*, 2017, **214**, 1600947.
- T. Honold, K. Volk, A. Rauh, J. P. S. Fitzgerald and M. Karg, *J. Mater. Chem. C*, 2015, **3**, 11449–11457.
- C. J. Kiely, J. Fink, M. Brust, D. Bethell and D. J. Schiffrin, *Nature*, 1998, **396**, 444–446.
- M. H. Kim, S. H. Im and O. O. Park, *Adv. Funct. Mater.*, 2005, **15**, 1329–1335.
- Z. Y. Cai, Y. J. Liu, X. M. Lu and J. H. Teng, *ACS Appl. Mater. Interfaces*, 2014, **6**, 10265–10273.
- D. Taha, S. K. Mkhonta, K. R. Elder and Z. F. Huang, *Phys. Rev. Lett.*, 2017, **118**, 255501.
- K. S. Khalil, A. Sagastegui, Y. Li, M. A. Tahir, J. E. S. Socolar, B. J. Wiley and B. B. Yellen, *Nat. Commun.*, 2012, **3**, 794.
- M. Karg, T. A. F. König, M. Retsch, C. Stelling, P. M. Reichstein, T. Honold, M. Thelakkat and A. Fery, *Mater. Today*, 2015, **18**, 185–205.
- M. Mayer, M. J. Schnepf, T. A. F. König and A. Fery, *Adv. Opt. Mater.*, 2019, **7**, 1800564.
- M. Müller, M. Tebbe, D. V. Andreeva, M. Karg, R. A. Alvarez-Puebla, N. Pazos-Perez and A. Fery, *Langmuir*, 2012, **28**, 9168–9173.
- M. Dridi and G. C. Schatz, *J. Opt. Soc. Am. B*, 2015, **32**, 818.
- A. H. Schokker and A. F. Koenderink, *Phys. Rev. B*, 2014, **90**, 155452.
- M. I. Stockman, *NPG Asia Mater.*, 2013, **5**, e71.
- A. Yang, T. B. Hoang, M. Dridi, C. Deeb, M. H. Mikkelsen, G. C. Schatz and T. W. Odom, *Nat. Commun.*, 2015, **6**, 6939.
- W. Zhou, M. Dridi, J. Y. Suh, C. H. Kim, D. T. Co, M. R. Wasielewski, G. C. Schatz and T. W. Odom, *Nat. Nanotechnol.*, 2013, **8**, 506–511.
- N. Vogel, L. de Viguier, U. Jonas, C. K. Weiss and K. Landfester, *Adv. Funct. Mater.*, 2011, **21**, 3064–3073.
- N. Vogel, S. Goerres, K. Landfester and C. K. Weiss, *Macromol. Chem. Phys.*, 2011, **212**, 1719–1734.
- M. Retsch, Z. C. Zhou, S. Rivera, M. Kappl, X. S. Zhao, U. Jonas and Q. Li, *Macromol. Chem. Phys.*, 2009, **210**, 230–241.
- M. E. J. Hummel, C. Stelling, B. A. F. Kopera, F. A. Nutz, M. Karg, M. Retsch and S. Forster, *Langmuir*, 2019, **35**, 973–979.
- N. Hoffmann, F. Ebert, C. N. Likos, H. Löwen and G. Maret, *Phys. Rev. Lett.*, 2006, **97**, 078301.
- S. Deutschländer, T. Horn, H. Löwen, G. Maret and P. Keim, *Phys. Rev. Lett.*, 2013, **111**, 098301.
- S. Deutschländer, P. Dillmann, G. Maret and P. Keim, *Proc. Natl. Acad. Sci. U. S. A.*, 2015, **112**, 6925–6930.
- H. Löwen, T. Horn, T. Neuhaus and B. ten Hagen, *Eur. Phys. J.: Spec. Top.*, 2013, **222**, 2961–2972.
- M. Karg, A. Pich, T. Hellweg, T. Hoare, L. A. Lyon, J. J. Crassous, D. Suzuki, R. A. Gumerov, S. Schneider, I. I. Potemkin and W. Richtering, *Langmuir*, 2019, **35**, 6231–6255.
- F. Camerin, M. A. Fernandez-Rodriguez, L. Rovigatti, M. N. Antonopoulou, N. Gnan, A. Ninarello, L. Isa and E. Zaccarelli, *ACS Nano*, 2019, **13**, 4548–4559.
- M. Karg, *Colloid Polym. Sci.*, 2012, **290**, 673–688.
- M. Karg, *Macromol. Chem. Phys.*, 2016, **217**, 242–255.
- T. Honold, K. Volk, M. Retsch and M. Karg, *Colloids Surf., A*, 2016, **510**, 198–204.
- M. Á. Fernández-Rodríguez, R. Elnathan, R. Ditcovski, F. Grillo, G. M. Conley, F. Timpu, A. Rauh, K. Geisel, T. Ellenbogen, R. Grange, F. Scheffold, M. Karg, W. Richtering, N. H. Voelcker and L. Isa, *Nanoscale*, 2018, **10**, 22189–22195.
- B. V. Enüstün and J. Turkevich, *J. Am. Chem. Soc.*, 1963, **85**, 3317–3328.
- A. Rauh, T. Honold and M. Karg, *Colloid Polym. Sci.*, 2016, **294**, 37–47.
- K. Volk, J. P. S. Fitzgerald and M. Karg, *ACS Appl. Mater. Interfaces*, 2019, **11**, 16096–16106.
- A. Lang, G. Kahl, C. N. Likos, H. Löwen and M. Watzlawek, *J. Phys.: Condens. Matter*, 1999, **11**, 10143–10161.
- A. R. Denton and H. Löwen, *J. Phys.: Condens. Matter*, 1997, **9**, L1–L5.
- J. Fornleitner and G. Kahl, *EPL*, 2008, **82**, 18001.
- H. Pattabhiraman, A. P. Gantapara and M. Dijkstra, *J. Chem. Phys.*, 2015, **143**, 164905.
- H. Pattabhiraman and M. Dijkstra, *J. Phys.: Condens. Matter*, 2017, **29**, 094003.
- H. G. Schoberth, H. Emmerich, M. Holzinger, M. Dulle, S. Förster and T. Gruhn, *Soft Matter*, 2016, **12**, 7644–7654.
- T. Kureha, H. Minato, D. Suzuki, K. Urayama and M. Shibayama, *Soft Matter*, 2019, **15**, 5390–5399.

- 52 M. P. Allen and D. J. Tildesley, *Computer Simulation of Liquids*, Oxford Scholarship Online, 2017.
- 53 R. Pelton, *Adv. Colloid Interface Sci.*, 2000, **85**, 1–33.
- 54 M. Shibayama, T. Tanaka and C. C. Han, *J. Chem. Phys.*, 1992, **97**, 6829–6841.
- 55 S. Höfl, L. Zitzler, T. Hellweg, S. Herminghaus and F. Mugele, *Polymer*, 2007, **48**, 245–254.
- 56 S. Hirotsu, Y. Hirokawa and T. Tanaka, *J. Chem. Phys.*, 1987, **87**, 1392–1395.
- 57 S. A. Vasudevan, A. Rauh, L. Barbera, M. Karg and L. Isa, *Langmuir*, 2018, **34**, 886–895.
- 58 A. Rauh, M. Rey, L. Barbera, M. Zanini, M. Karg and L. Isa, *Soft Matter*, 2016, **13**, 158–169.
- 59 S. A. Vasudevan, A. Rauh, M. Kroger, M. Karg and L. Isa, *Langmuir*, 2018, **34**, 15370–15382.
- 60 M. B. Müller, C. Kuttner, T. A. König, V. V. Tsukruk, S. Förster, M. Karg and A. Fery, *ACS Nano*, 2014, **8**, 9410–9421.
- 61 K. Geisel, W. Richtering and L. Isa, *Soft Matter*, 2014, **10**, 7968–7976.
- 62 A. Reinmüller, H. J. Schöpe and T. Palberg, *Soft Matter*, 2010, **6**, 5312–5315.
- 63 W. A. Goedel, K. Glaser, D. Mitra, J. Hammerschmidt, R. Thalheim, P. Ueberfuhr and R. R. Baumann, *Langmuir*, 2019, **35**, 2196–2208.
- 64 F. Yan and W. A. Goedel, *Chem. Mater.*, 2004, **16**, 1622–1626.
- 65 K. Stratford, R. Adhikari, I. Pagonabarraga, J. C. Desplat and M. E. Cates, *Science*, 2005, **309**, 2198–2201.
- 66 R. E. Guerra, C. P. Kelleher, A. D. Hollingsworth and P. M. Chaikin, *Nature*, 2018, **554**, 346–350.
- 67 H. L. Liang, S. Schymura, P. Rudquist and J. Lagerwall, *Phys. Rev. Lett.*, 2011, **106**, 247801.
- 68 D. J. Kraft, R. Wittkowski, B. ten Hagen, K. V. Edmond, D. J. Pine and H. Löwen, *Phys. Rev. E*, 2013, **88**, 050301(R).